ACSNANO

www.acsnano.org

Realization of Symmetry-Enforced Two-Dimensional Dirac Fermions in Nonsymmorphic α-Bismuthene

Pawel J. Kowalczyk,* Simon A. Brown,* Tobias Maerkl, Qiangsheng Lu, Ching-Kai Chiu, Ying Liu, Shengyuan A. Yang, Xiaoxiong Wang, Ilona Zasada, Francesca Genuzio, Tevfik Onur Menteş, Andrea Locatelli, Tai-Chang Chiang, and Guang Bian*

Cite This: *ACS Nano* 2020, 14, 1888−1894

Read Online

ACCESS | Metrics & More | Article Recommendations | Supporting Information

ABSTRACT: **Two-dimensional (2D) Dirac-like electron gases have attracted tremendous research interest ever since the discovery of free-standing graphene. The linear energy dispersion and nontrivial Berry phase play a pivotal role in the electronic, optical, mechanical, and chemical properties of 2D Dirac materials. The known 2D Dirac materials are gapless only within certain approximations, for example, in the absence of spin−orbit coupling (SOC). Here, we report a route to establishing robust Dirac cones in 2D materials with nonsymmorphic crystal lattice. The nonsymmorphic symmetry enforces Dirac-like band dispersions around certain high-symmetry momenta in the presence of SOC. Through μ-ARPES measurements, we observe Dirac-like band dispersions in α-bismuthene. The nonsymmorphic lattice symmetry is confirmed by μ-low-energy electron diffraction and scanning tunneling microscopy. Our first-principles simulations and theoretical topological analysis demonstrate the correspondence between nonsymmorphic symmetry and Dirac states. This mechanism can be straightforwardly generalized to other nonsymmorphic materials. The results enlighten the search of symmetry-enforced Dirac fermions in the vast uncharted world of nonsymmorphic 2D materials.**

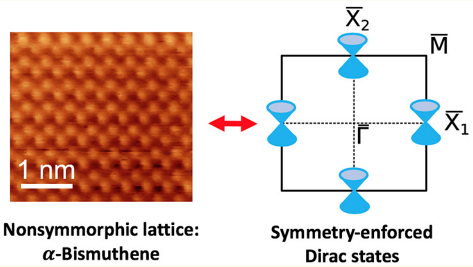

KEYWORDS: *Dirac materials, symmetry-enforced states, nonsymmorphic symmetry, bismuthene, spin−orbit coupling*

The discovery of graphene and topological insulators has stimulated enormous interest in two-dimensional (2D) electron gas with linear band dispersion.[1−3] The vanishing effective mass and nonzero Berry phase of Dirac fermion-like states give rise to many interesting physical properties such as extremely high mobilities and zero-energy Landau levels.[4] The two-dimensional Dirac cones are generally fragile against perturbations, and so various gapped electronic phases are observed.[5] For example, the weak spin−orbit coupling (SOC) can make graphene a quantum spin Hall insulator. Gapless 2D Dirac fermions can be found on the surfaces of 3D topological insulators.[3] However, when the dimension of the 3D systems is reduced, a tunneling energy gap opens at the Dirac point due to the hybridization of the surface states on the opposite surfaces. Therefore, it is a highly challenging task to find gapless Dirac fermions in intrinsic 2D materials. So far, only a few 2D materials have been theoretically predicted to possess Dirac states, including graphene,[1,2] silicene,[6] germanene,[7] and some artificial structures.[8−11] Among them, only graphene has been experimentally proven to possess Dirac cones as the spin−orbit gap is negligibly small.

The reason for the rarity of 2D Dirac materials can be seen from a simple co-dimension analysis. The general Hamiltonian of 2D Dirac states is described by $\alpha\sigma_x k_x + \beta\sigma_y k_y$, where σ_i and k_i are Pauli matrices and momentum components, and α and β are constants. The Dirac cone can be easily gapped by any perturbations in the form of $m\sigma_z$, and the resulting gapped system is energetically favored given that the Fermi level is in the gap. The perturbation can be from the intrinsic SOC of the system, as in graphene, or from lattice relaxations which reduce the surface energy of the 2D material.[12] In order to achieve truly gapless Dirac dispersion, geometrical or topological constraints are required to eliminate the gap term. Previous theoretical studies of the relation between lattice symmetry

Received: October 15, 2019
Accepted: January 23, 2020
Published: January 23, 2020

and Dirac states suggested that nonsymmorphic symmetries can enforce Dirac-like band structures.[13−17] The key idea is that the operator algebra involving nonsymmorphic symmetries allows only nontrivial irreducible representations at certain high-symmetry points of the Brillouin zone.[15,17] However, to date, a material realization of symmetry-enforced Dirac fermions in 2D nonsymmorphic materials is still elusive.

In this work, we report the existence of 2D Dirac fermions in α-bismuthene ("α-Bi" for short). The Dirac band structure is observed by our micro-angle-resolved photoemission spectroscopy (μ-ARPES) experiment. The Dirac cone is protected by the glided mirror of the nonsymmorphic α-bismuthene lattice and shows that this concept can be generalized to other 2D materials with nonsymmorphic layer groups. The Dirac points are located at certain high-symmetry momentum points which are entirely determined by the symmetry of the lattice. This correspondence of Dirac states to the lattice symmetry can accelerate discovery of a wide range of 2D Dirac materials. In this paper, we first report our experimental results on α-bismuthene. Then we will present a theoretical analysis of the 2D Dirac cone in this material as well as the first-principles band structure of bismuthene films. Finally, we discuss a guiding rule for the search of 2D Dirac materials.

RESULTS AND DISCUSSION

In our experiment, α-Bi was grown by thermal evaporation of bismuth (99.999%) onto the highly oriented pyrolytic graphite (HOPG) substrate. The HOPG substrate was cleaved before deposition, annealed in UHV at 750 K for several hours to remove contaminants, and then kept at room temperature during deposition. In Figure 1a, a typical low-energy electron microscopy (LEEM) image recorded on α-Bi is shown. α-Bi is relatively well-characterized and consists of two-monolayer-thick butterfly-like bases with black phosphorus-like crystallographic structure and the (110) plane (rhombohedral indices) parallel to the substrate[18,19] (see Figure 1b). On top of α-Bi, additional stripes of α-Bi are usually observed. These can be seen in LEEM images due to quantum oscillations in electron reflectivity for electron energies below 10 eV (as a result of the long inelastic mean free path). In our experiments, we found that highest height contrast for Bi on HOPG is obtained for electron energy equal to 8 eV (see Figure 1a).

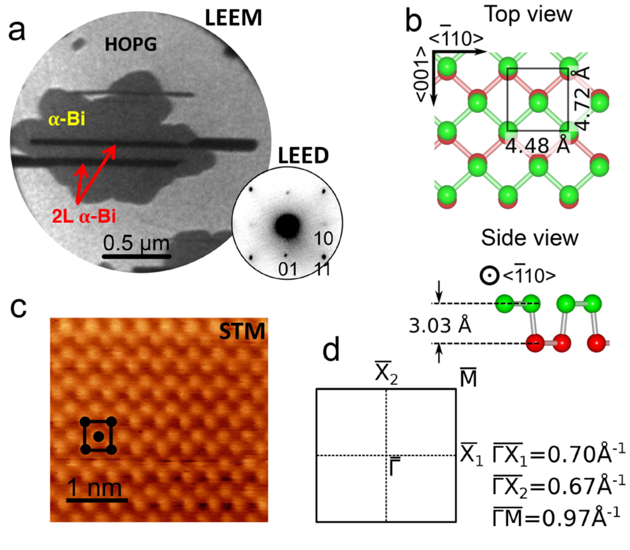

Figure 1. LEEM and scanning transmission microscopy (STM) results recorded on α-bismuthene (a) LEEM image of the α-Bi island. Micro-low-energy electron diffraction (μ-LEED) pattern recorded on α-Bi island is shown in the inset. (b) Lattice structure of α-Bi belonging to the #42 layer group *pman*: top and side views. The Bi atoms at two different heights are colored in red and green. The dimension of the unit cell after full density functional theory optimization is shown. (c) Atomic-resolution STM image of α-Bi. (d) Brillouin zone of α-Bi.

By using micro-low-energy electron diffraction (μ-LEED) (aperture size 500 nm), we confirm that the crystallographic structure of these islands is of black-phosphorus-type (see top inset in Figure 1a, recorded on an island shown in Figure 1a) rather than, for example, possible hexagonal structures.[20,21] Close inspection of the μ-LEED pattern reveals the very weak intensity of the (10) spots, which is the result of glide-line symmetry along the $\langle\bar{1}10\rangle$ direction[22] (in rhombohedral indices, for a ball-and-stick model, see Figure 1b). Detailed analysis on the LEED intensity pattern indicates that the two atoms in each layer in the unit cell are at nearly the same height; the surface buckling is small, with a deformation Δz around 0.04 ± 0.005 Å; please see the Supporting Information for a detailed discussion. The geometry of the unit cell from the LEED fitting is shown in Figure 1b. This structure belongs to the #42 layer group (*pman*). The dimensions of the unit cell from scanning tunneling microscopy (STM) measurements are $(4.5 \pm 0.2) \times (4.8 \pm 0.2)$ Å^2; see Figure 1c. The two-atom surface unit cell from STM is consistent with the LEED result. This is further supported by our fully relaxed first-principles calculations (in the framework of density functional theory (DFT)) performed for a free-standing film, yielding a unit cell of 4.48×4.72 Å^2 (see Figure 1b). Note that in this structure there is no buckling within the uncertainties of the calculations; that is, the atoms in each layer are exactly parallel to the surface plane; please see a detailed discussion in the Supporting Information. The Brillouin zone is plotted in Figure 1d, in which $\bar{\Gamma}-\bar{X}_1$ is along the $\langle\bar{1}10\rangle$ direction and $\bar{\Gamma}-\bar{X}_2$ along the $\langle 001\rangle$ direction.

In order to understand the electronic properties of α-Bi, we performed μ-ARPES measurements using a spectroscopic photoemission and low-energy electron microscope (SPELEEM)[23] on the island shown in Figure 1a. When operated in the diffraction imaging mode, the SPELEEM microscope can record the ARPES pattern up to $k_{\|}$ such that the first and a large portion of the second Brillouin zones of α-Bi are imaged. Results of μ-ARPES experiments are compared with DFT calculations in Figure 2 along the high-symmetry directions of the surface Brillouin zone. Second derivative procedures are used to enhance the visibility of the band features (smoothing and moving average used before second derivative calculation), as in the central column of Figure 2. α-Bi is a semiconductor with the Fermi level barely touching the top of the valence band, as shown in the ARPES spectra. The most prominent feature of the valence band is that band crossings exist at $\bar{X}_1$ and $\bar{X}_2$. A band degeneracy occurs for every band crossing at these two high-symmetry points. Here, we focus on the band crossings at 0.7 and 0.4 eV (denoted by "DP1" and "DP2", respectively, in Figure 2) as examples and present a detailed analysis of the band dispersion. The conclusions from this analysis apply to every pair of bands that cross at $\bar{X}_1$ and $\bar{X}_2$. Overall, the agreement between theory and experiment is good considering the ARPES spectrum is taken from a single α-Bi island with size about 1 μm × 1 μm. We note that there are no spectral features ascribed to the HOPG substrate because, in

https://dx.doi.org/10.1021/acsnano.9b08136
ACS Nano 2020, 14, 1888−1894

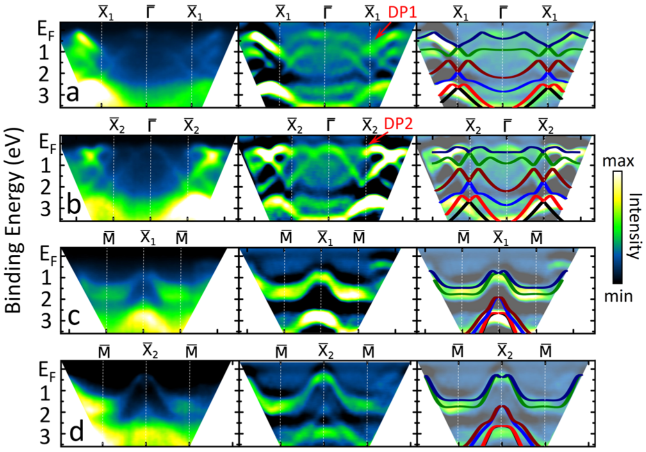

Figure 2. *μ*-ARPES band structure taken from a single island of *α*-Bi. (a−d) ARPES band mapping taken at photon energy 27.9 eV along different high-symmetry directions, as indicated in each panel. The raw data are shown in the left column, second-derivative enhanced data in the middle, and ARPES result overlaid with first-principles bands in the right column.

the vicinity of Fermi level, HOPG bands are located farther away from the center of the Brillouin zone.

The agreement between experiment and theory is seen very clearly in the plots of iso-energy contours (see Figure 3a). The calculated contours are plotted on top of experimental images for comparison. In the first Brillouin zone, there are four small hole pockets at 0.2 eV, two of which are in between $\bar{\Gamma}$ and $\bar{X}_1$ and the other two close to $\bar{X}_2$. In the vicinity of $\bar{X}_2$, the two hole pockets grow into a star-shaped contour (indicated by arrows in the middle panel of Figure 3a) as the binding energy goes from 0.2 to 0.4 eV. The center of the star corresponds to the Dirac point DP2 located at $\bar{X}_2$. The two pockets between $\bar{\Gamma}$ and $\bar{X}_1$ also grow larger as the binding energy increases, and at 0.7 eV, they touch the pockets in the second Brillouin zone at $\bar{X}_1$, forming the Dirac point DP1 (see the bottom panel of Figure 3a). These pockets eventually merge together into squarish contours for higher binding energy values (see the iso-energy contours at 0.9, 1.2, and 1.4 eV in Figure 3a). This evolution of band contours is consistent with the DFT simulations. The DFT band structure in Figure 3b demonstrates the band crossings DP1 and DP2. Figure 3c,d shows 3D representations of the bands obtained from ARPES and DFT calculation, respectively. To compare with the experimental result, the DFT bands are smeared out by 0.5 eV. All main features in the ARPES data are well reproduced by DFT calculations, strongly suggesting the existence of nonsymmorphic Dirac states. In particular, the band crossing features marked by arrows are nearly identical, which indicates that a Dirac state indeed exists at $\bar{X}_1$. We note that the Dirac bands at DP1 and DP2 are anisotropic, especially along $\bar{X}_2-\bar{M}$ direction. The linear dispersion can be seen only in the close vicinity of $\bar{X}_1$ and $\bar{X}_2$, as shown in Figure 4a,b.

According to the ARPES and first-principles results, Dirac cones exist at $\bar{X}_1 = (\pi,0)$ and $\bar{X}_2 = (0,\pi)$ of the Brillouin zone (for simplicity, the lengths are measured in units of the lattice constants a_x and a_y along $\langle\bar{1}10\rangle$ and $\langle 001\rangle$ directions, respectively). We now show that these band degeneracies are protected by the nonsymmorphic lattice symmetry. α-Bi is nonmagnetic and centrosymmetric, so the time reversal (T) and inversion (P) symmetries are preserved. (Note again the lack of buckling.) The space−time inversion symmetry PT leads to the two-fold Kramers degeneracy of each band in the Brillouin zone in the presence of SOC. Therefore, the band degeneracy is 4 for the band crossing points at $\bar{X}_1$ and $\bar{X}_2$. The lattice of α-bismuthene belongs to the #42 layer group ($pman$), which is described by the three generators:

$$\tilde{M}_z\colon (x + 1/2, y + 1/2, -z)i\sigma_z \tag{1}$$

$$P\colon (-x, -y, -z)\sigma_0 \tag{2}$$

$$M_x\colon (-x, y, z)i\sigma_x \tag{3}$$

where σ_i ($i = x, y, z$) are Pauli matrices for the spin degree of freedom and σ_0 is the 2 × 2 identity matrix. Here, the tilde in $\tilde{M}_z$ indicates that it is a nonsymmorphic glide mirror operation—the mirror reflection is accompanied by a half-lattice translation parallel to the mirror plane. We shall see that the three symmetries $\tilde{M}_z$, P, and T dictate the existence of Dirac points at $\bar{X}_1$ and $\bar{X}_2$, which are robust under SOC.

We first show that the three symmetries guarantee four-fold band degeneracies at $\bar{X}_1$ and $\bar{X}_2$. The key point is that the nonsymmorphic character of $\tilde{M}_z$ leads to a special commutation relation between $\tilde{M}_z$ and P. To see this, we

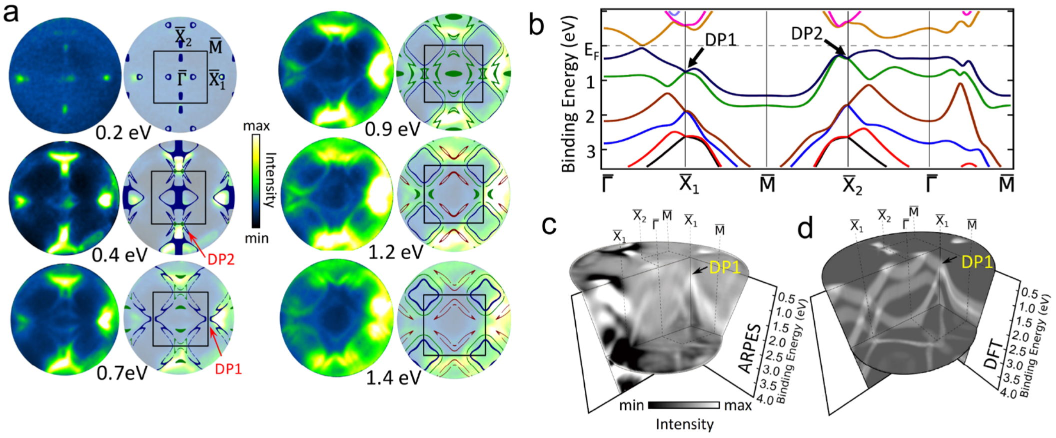

Figure 3. *μ*-ARPES iso-energy contours and first-principles simulations. (a) *μ*-ARPES iso-energy contours taken at binding energy of 0.2, 0.4, 0.7, 0.9, 1.2, and 1.4 eV. (b) DFT-calculated bands for *α*-Bi. (c) 3D band representation with two cross-sectional planes $\bar{X}_1-\text{M}-\bar{X}_1$ and $\bar{X}_1-\bar{\Gamma}-\bar{X}_1$. (d) Corresponding calculated 3D band contour with smearing of 0.5 eV.

https://dx.doi.org/10.1021/acsnano.9b08136
ACS Nano 2020, 14, 1888−1894

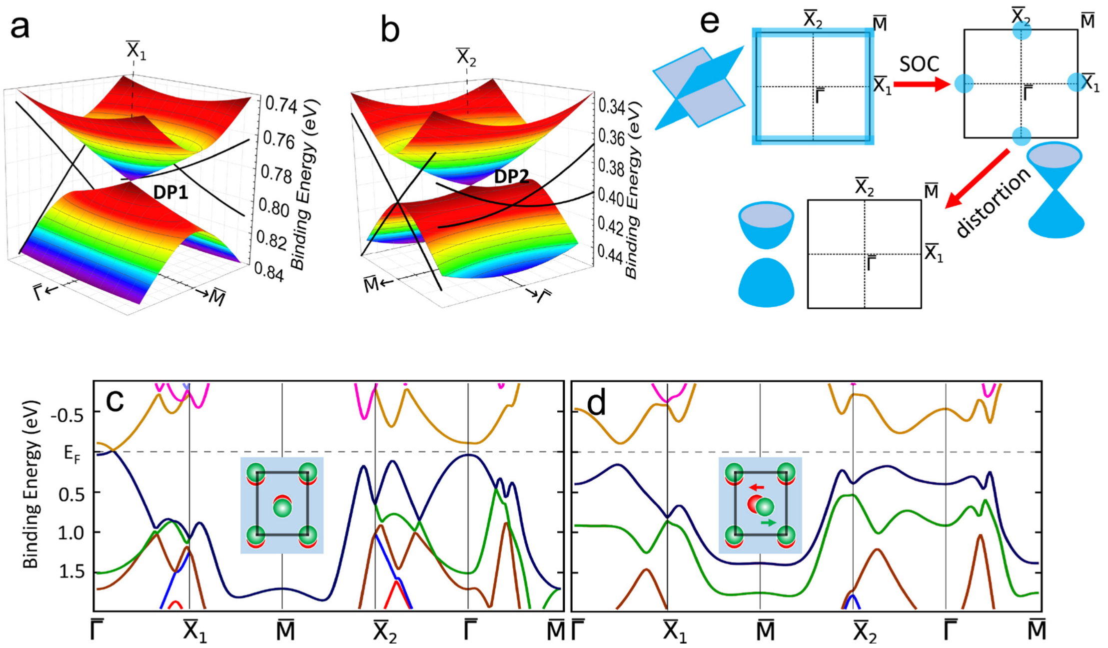

Figure 4. SOC and distortion effects on α-Bi band structure. (a,b) DFT band surface calculated in the vicinity of $\bar{X}_1$ and $\bar{X}_2$, respectively. (c) Band structure of α-Bi in the absence of spin−orbit coupling. (d) Band structure of distorted α-Bi. The distortion is shown in the inset. The two atoms are moved along arrow directions by 2% of the unit cell width. (e) Evolution of band configuration from without SOC to with SOC to with both SOC and symmetry-breaking distortion. The Dirac/nodal points are highlighted in blue in the Brillouin zone.

compare the results when these two symmetry operators act on (x, y, z) in the different orders:

$$(x, y, z) \xrightarrow{P} (-x, -y, -z) \xrightarrow{\tilde{M}_z} (-x + 1/2, -y + 1/2, z) \tag{4}$$

$$(x, y, z) \xrightarrow{\tilde{M}_z} (x + 1/2, y + 1/2, -z) \xrightarrow{P} (-x - 1/2, -y - 1/2, z) \tag{5}$$

This means that

$$\tilde{M}_z P = T_{110} P \tilde{M}_z \tag{6}$$

where $T_{110} = e^{-ik_x - ik_y}$ denotes the translation by one unit cell along both x and y directions. Consequently, at the special high-symmetry points $\bar{X}_1$: $(\pi,0)$ and $\bar{X}_2$: $(0,\pi)$, $\tilde{M}_z$ and P anticommute with each other: $\{\tilde{M}_z, P\} = 0$. Meanwhile, the nonsymmorphic character also makes the eigenvalues of $\tilde{M}_z$ momentum-dependent. As $(\tilde{M}_z)^2 = -T_{110}$ (the minus sign is due to a 2π rotation on spin), we have the $\tilde{M}_z$ eigenvalues $g_z = \pm ie^{-ik_x/2 - ik_y/2}$. Importantly, at $\bar{X}_1$ and $\bar{X}_2$, $g_z = \pm 1$, which is purely real.

Consider an energy eigenstate $|\Phi(\bar{X}_i)\rangle$ at $\bar{X}_i$ $(i = 1, 2)$, which can be chosen as an eigenstate of $\tilde{M}_z$ with an eigenvalue g_z. As $\bar{X}_i$ is a T-invariant momentum point, $|\Phi(\bar{X}_i)\rangle$ has a degenerate Kramers partner $T|\Phi(\bar{X}_i)\rangle$, which must share the same g_z eigenvalue (because $g_z = \pm 1$ is real). Moreover, because $\{\tilde{M}_z, P\} = 0$, $P|\Phi(\bar{X}_i)\rangle$ (and also $TP|\Phi(\bar{X}_i)\rangle$) must be another degenerate partner of $|\Phi(\bar{X}_i)\rangle$ with an *opposite* $\tilde{M}_z$ eigenvalue $(-g_z)$. Thus, the four states $(|\Phi\rangle, P|\Phi\rangle, T|\Phi\rangle, TP|\Phi\rangle)$ always form a degenerate quartet at $\bar{X}_1$ and $\bar{X}_2$. Deviating from $\bar{X}_i$, the four-fold degeneracy will generally be lifted because the k point is no longer invariant under T. We note that eq 6 plays the pivotal role in the formation of band degeneracy. The phase factor from T_{110}, reflecting the nonsymmorphic nature of the lattice, determines the existence and location of the Dirac points. In addition, the above argument is made with explicit consideration of SOC, so these Dirac points are indeed robust against SOC and can be termed as the 2D spin−orbit Dirac points.

To further characterize the emergent 2D spin−orbit Dirac fermions and to show that the dispersion is indeed a linear type, we construct an effective $k{\cdot}p$ model around each Dirac point based on the symmetry constraints. Consider DP1 at $\bar{X}_1$, the symmetry operations in the little group at $\bar{X}_1$ include T and the three generators in eqs 1−3. The matrix representations of these operators can be obtained from the standard reference,[24] with $T = -i\sigma_y \otimes \tau_0 K$, $\tilde{M}_z = \sigma_z \otimes \tau_y$, $P = \sigma_0 \otimes \tau_x$, and $M_x = -i\sigma_x \otimes \tau_x$. Here, K is the complex conjugation operator, σ_j and τ_j ($j = x, y, z$) are the Pauli matrices representing spin and orbital degrees of freedom, respectively, and σ_0 and τ_0 are the 2×2 identity matrices. Subjected to these symmetry constraints, the effective model in the vicinity of DP1 expanded to linear order in the wave vector k' takes the form of

$$\mathcal{H}(\boldsymbol{k}') = v_x k_x'(\cos\theta\, \sigma_x \otimes \tau_z + \sin\theta\, \sigma_0 \otimes \tau_y) + v_y k_y' \sigma_y \otimes \tau_z \tag{7}$$

where the energy and the wave vector $\boldsymbol{k}' = (k_x', k_y')$ are measured from DP1, the model parameters v_x, v_y, and θ are real, and their values depend on the microscopic details. The dispersion around DP1 is given by $E = \pm\sqrt{v_x^2 k_x'^2 + v_y^2 k_y'^2}$, which indeed corresponds to a linear Dirac cone. This confirms that the emergent fermions are 2D spin−orbit Dirac fermions.

The effective model for DP2 at $\bar{X}_2$ can be defined in a similar way. With $T = -i\sigma_y \otimes \tau_0 K$, $\tilde{M}_z = \sigma_z \otimes \tau_y$, $P = \sigma_0 \otimes \tau_x$, and $M_x = -i\sigma_x \otimes \tau_0$, the effective Hamiltonian can be written as

$$\mathcal{H}(\boldsymbol{k}') = v_x k_x' \sigma_y \otimes \tau_z + v_y k_y'(\cos\theta\, \sigma_x \otimes \tau_z + \sin\theta\, \sigma_0 \otimes \tau_y) \tag{8}$$

Because there is no symmetry operation connecting DP1 and DP2, the model parameters are generally different for DP1 and DP2. For example, from fitting the DFT band structure, at DP1, we find the Fermi velocities $v_x = 3.95 \times 10^5$ m/s and $v_y =$

https://dx.doi.org/10.1021/acsnano.9b08136
ACS Nano 2020, 14, 1888−1894

2.12×10^5 m/s, whereas at DP2, $v_x = 1.19 \times 10^5$ m/s and $v_y = 4.67 \times 10^5$ m/s. The lack of symmetry connection implies that each Dirac point may be tuned separately. For example, a single Dirac point may be tuned close to the Fermi level by lattice deformations that preserve the crystal symmetry. This is in contrast to the case of graphene, where the two Dirac points are symmetry-connected and hence must shift in energy together.

The strong spin−orbit coupling in α-Bi is crucial for the formation of the nonsymmorphic Dirac states. To see this, we calculated the band structure without the inclusion of SOC; the result is shown in Figure 4c. The bands become degenerate along $\bar{X}_1-\bar{M}-\bar{X}_2$ and, consequently, form a nodal line at the boundary of the Brillouin zone; see Figure 4e. The band degeneracy is also due to the nonsymmorphic symmetry of the lattice (please see the Supporting Information for details). However, this band degeneracy is not robust against spin−orbit coupling. Turning on SOC, the nodal line is gapped everywhere except $\bar{X}_1$ and $\bar{X}_2$. In other words, SOC transforms the system from a nodal-line system into a Dirac fermion state. In the presence of SOC, the Dirac points at $\bar{X}_1$ and $\bar{X}_2$ are under the protection of the glided mirror symmetry. Naturally, breaking this glided mirror symmetry will lead to energy gaps at the Dirac points. Figure 4d shows the band structure of a distorted lattice. The lattice distortion is depicted in the inset of Figure 4d, which destroys the glided mirror symmetry while keeping the space inversion symmetry. In this case, every band still possesses the two-fold Kramers degeneracy, but the Dirac points at $\bar{X}_1$ and $\bar{X}_2$ disappear. This evolution of band surfaces and Dirac/nodal points, as schematically depicted in Figure 4e, indicates that SOC and nonsymmorphic symmetry are two essential pillars supporting the formation of Dirac fermions in α-Bi.

CONCLUSIONS

α-Bismuthene, a two-dimensional spin−orbit material, hosts Dirac fermion states at the high-symmetry momentum points $\bar{X}_1$ and $\bar{X}_2$, as demonstrated by our μ-ARPES measurements and first-principles calculations. The band degeneracy at the Dirac points are strictly protected by the nonsymmorphic symmetry of the lattice. Unlike graphene and other known 2D Dirac materials, the nonsymmorphic symmetry guarantees that the Dirac states in α-bismuthene are robust against spin−orbit coupling. Breaking the lattice symmetry, on the other hand, can lift the band degeneracy at Dirac points and yield gapped phases. Interestingly, a surface buckling in α-bismuthene breaks the space inversion symmetry and turns the system into a 2D elemental ferroelectric.[25] Moreover, the two allotropic phases of bismuthene, namely, α-Bi and β-Bi, possess nontrivial band topology. The β-Bi was first theoretically proposed to be a quantum spin Hall (QSH) insulator and recently realized in experiment.[26,27] Similar to the β phase, α-Bi has been reported to be a QSH in its flat form.[28] Here, we confirm the α-bismuthene prepared on HOPG is with negligible surface buckling and, therefore, belongs to the QSH topological phase.

The formation mechanism of Dirac bands discussed in this work is intrinsically different from the band crossing induced by nonsymmorphic crystalline symmetry reported in previous works.[29−33] The two bands exchange the eigenvalues of a single nonsymmorphic operator, a glided plane or a screw axis, as they disperse from one high-symmetry momentum to another high-symmetry momentum. Therefore, a band crossing must happen between the two high-symmetry points. By contrast, the Dirac points in α-bismuthene reside at the high-symmetry momenta of the Brillouin zone because these points are invariant under P and T and allow momentum-dependent commutation/anticommutation relations involving the nonsymmorphic symmetry operators. In other words, the location of the Dirac points is determined by the nonsymmorphic symmetry operations.[15] This property facilitates the detection of Dirac states in experiments. For example, let us consider a different nonsymmorphic group, the #15 layer group ($p2_1/m11$). A bismuth monolayer structure belongs to this layer group (please see the Supporting Information). Because of a screw axis of the lattice, Dirac states are guaranteed to exist at $\bar{X}_1$ and $\bar{M}$ points of the Brillouin zone. The principle demonstrated in this work can be applied to all 2D layered materials with a lattice belonging to one of the 36 nonsymmorphic layer groups.[15,17] This will significantly accelerate the search of 2D Dirac materials and extend "graphene" physics into the territory where strong spin−orbit coupling is present.

METHODS

Commercially available HOPG (SPI-1) was used as a substrate in all experiments. It was cleaved in air, loaded into the UHV system, and annealed at 700−900 K for several hours to remove contaminants. After the substrate cooled to room temperature, high-purity bismuth (99.999%) was evaporated from a ceramic crucible and deposited onto the substrate at rates of ~0.01 Å/s.

LEEM, μ-LEED, and μ-ARPES measurements were performed at room temperature and base pressure of 10^{-9} Pa with the spectroscopic photoemission and low-energy electron microscope installed at the Nanospectroscopy Beamline of the Elettra Synchrotron Laboratory (Italy).[23]

Soft X-rays at an energy of 27.9 eV were used for μ-ARPES measurements. Kinetic electron energies were analyzed using a hemispherical band-pass energy filter (operating with pass energy of 908 eV). Apertures 500 and 2000 nm wide were used for μ-LEED and μ-ARPES measurements, respectively.

First-principles calculations of the electronic structure of the films were performed using Hartwigsen−Goedecker−Hutter-type pseudopotentials[34] and a plane-wave basis set. The main program employed was developed by the ABINIT group.[35] Spin−orbit coupling was included using the relativistic local density approximation.

ASSOCIATED CONTENT

Supporting Information

The Supporting Information is available free of charge at https://pubs.acs.org/doi/10.1021/acsnano.9b08136.

> Detailed analysis on experimental results and lattice symmetries (PDF)

AUTHOR INFORMATION

Corresponding Authors

Pawel J. Kowalczyk − *Department of Solid State Physics, Faculty of Physics and Applied Informatics, University of Lodz, 90-236 Lodz, Poland;* orcid.org/0000-0001-6310-4366; Email: pawel.kowalczyk@uni.lodz.pl

Simon A. Brown − *The MacDiarmid Institute for Advanced Materials and Nanotechnology, School of Physical and Chemical Sciences, University of Canterbury, Christchurch 8140, New Zealand;* Email: simon.brown@canterbury.ac.nz

Guang Bian − *Department of Physics and Astronomy, University of Missouri, Columbia, Missouri 65211, United States;* orcid.org/0000-0001-7055-2319; Email: biang@missouri.edu

Authors

Tobias Maerkl − *The MacDiarmid Institute for Advanced Materials and Nanotechnology, School of Physical and Chemical Sciences, University of Canterbury, Christchurch 8140, New Zealand*

Qiangsheng Lu − *Department of Physics and Astronomy, University of Missouri, Columbia, Missouri 65211, United States*

Ching-Kai Chiu − *Kavli Institute for Theoretical Sciences, University of Chinese Academy of Sciences, Beijing 100190, China*

Ying Liu − *Research Laboratory for Quantum Materials, Singapore University of Technology and Design, Singapore 487372*

Shengyuan A. Yang − *Research Laboratory for Quantum Materials, Singapore University of Technology and Design, Singapore 487372*

Xiaoxiong Wang − *College of Science, Nanjing University of Science and Technology, Nanjing 210094, China*

Ilona Zasada − *Department of Solid State Physics, Faculty of Physics and Applied Informatics, University of Lodz, 90-236 Lodz, Poland*

Francesca Genuzio − *Elettra - Sincrotrone Trieste S.C.p.A., , I-34149 Trieste, Italy;* orcid.org/0000-0003-0699-2525

Tevfik Onur Menteş − *Elettra - Sincrotrone Trieste S.C.p.A., , I-34149 Trieste, Italy*

Andrea Locatelli − *Elettra - Sincrotrone Trieste S.C.p.A., , I-34149 Trieste, Italy;* orcid.org/0000-0002-8072-7343

Tai-Chang Chiang − *Department of Physics and Frederick Seitz Materials Research Laboratory, University of Illinois at Urbana—Champaign, Urbana, Illinois 61801-3080, United States*

Complete contact information is available at:
https://pubs.acs.org/10.1021/acsnano.9b08136

Author Contributions

T.O.M., F.G., and A.L. performed all LEEM, LEED, and ARPES experiments, as well as the Bi growth and sample preparation, with the assistance of S.B., T.M., and P.J.K.; P.J.K. and I.Z. did LEED analyses; Q.L. and G.B. performed STM measurements; X.W., T.-C.C., and G.B. performed first-principles calculations; C.-K.C., S.A.Y., Y.L., and G.B. did theoretical analyses; P.J.K., S.A.B., and G.B. designed the project and wrote the manuscript. All authors discussed the manuscript.

Notes

The authors declare no competing financial interest.

A preprint version of this work can be found at https://arxiv.org/abs/1906.08456 (accessed Jun 20, 2019).

ACKNOWLEDGMENTS

This work was supported by the MacDiarmid Institute for Advanced Materials and Nanotechnology (S.A.B. and T.M.), the National Science Center, Poland (DEC-2015/17/B/ST3/02362, P.J.K.), the Singapore Ministry of Education Academic Research Fund Tier 2 (MOE2017-T2-2-108, S.A.Y.), the National Natural Science Foundation of China (11204133, X.X.W.), and the U.S. National Science Foundation (NSF-DMR-1305583, T.-C.C., and NSF-DMR-1809160, G.B.). The authors acknowledge P. Zielinski from UL for development of 3D ball-and-stick rendering software.

REFERENCES

(1) Novoselov, K. S.; Geim, A. K.; Morozov, S. V.; Jiang, D.; Katsnelson, M. I.; Grigorieva, I. V.; Dubonos, S. V.; Firsov, A. A. Two-Dimensional Gas of Massless Dirac Fermions in Graphene. *Nature* **2005**, *438*, 197−200.

(2) Zhang, Y.; Tan, Y.-W.; Stormer, H. L.; Kim, P. Experimental Observation of the Quantum Hall Effect and Berry's Phase in Graphene. *Nature* **2005**, *438*, 201−204.

(3) Hasan, M. Z.; Kane, C. L. *Colloquium*: Topological Insulators. *Rev. Mod. Phys.* **2010**, *82*, 3045−3067.

(4) Castro Neto, A. H.; Guinea, F.; Peres, N. M. R.; Novoselov, K. S.; Geim, A. K. The Electronic Properties of Graphene. *Rev. Mod. Phys.* **2009**, *81*, 109−162.

(5) Zhou, S. Y.; Siegel, D. A.; Fedorov, A. V.; Gabaly, F.; Schmid, A. K.; Neto, A. H. C.; Lee, D.-H.; Lanzara, A. Origin of the Energy Bandgap in Epitaxial Graphene. *Nat. Mater.* **2008**, *7*, 259.

(6) Zhao, J.; Liu, H.; Yu, Z.; Quhe, R.; Zhou, S.; Wang, Y.; Liu, C. C.; Zhong, H.; Han, N.; Lu, J.; Yao, Y.; Wu, K. Rise of Silicene: A Competitive 2D Material. *Prog. Mater. Sci.* **2016**, *83*, 24−151.

(7) Cahangirov, S.; Topsakal, M.; Akturk, E.; Sahin, H.; Ciraci, S. Two- and One-Dimensional Honeycomb Structures of Silicon and Germanium. *Phys. Rev. Lett.* **2009**, *102*, 236804.

(8) Malko, D.; Neiss, C.; Vines, F.; Görling, A. Competition for Graphene: Graphynes with Direction-Dependent Dirac Cones. *Phys. Rev. Lett.* **2012**, *108*, 086804.

(9) Zhou, X.-F.; Dong, X.; Oganov, A. R.; Zhu, Q.; Tian, Y.; Wang, H.-T. Semimetallic Two-Dimensional Boron Allotrope with Massless Dirac Fermions. *Phys. Rev. Lett.* **2014**, *112*, 085502.

(10) Gomes, K. K.; Mar, W.; Ko, W.; Guinea, F.; Manoharan, H. C. Designer Dirac Fermions and Topological Phases in Molecular Graphene. *Nature* **2012**, *483*, 306−310.

(11) Pardo, V.; Pickett, W. E. Half-Metallic Semi-Dirac-Point Generated by Quantum Confinement in TiO_2/VO_2 Nanostructures. *Phys. Rev. Lett.* **2009**, *102*, 166803.

(12) Bian, G.; Wang, X.; Miller, T.; Chiang, T.-C.; Kowalczyk, P. J.; Mahapatra, O.; Brown, S. A. First-Principles and Spectroscopic Studies of Bi(110) Films: Thickness-Dependent Dirac Modes and Property Oscillations. *Phys. Rev. B: Condens. Matter Mater. Phys.* **2014**, *90*, 195409.

(13) Young, S. M.; Kane, C. L. Dirac Semimetals in Two Dimensions. *Phys. Rev. Lett.* **2015**, *115*, 126803.

(14) Guan, S.; Liu, Y.; Yu, Z.-M.; Wang, S.-S.; Yao, Y.; Yang, S. A. Two-Dimensional Spin-Orbit Dirac Point in Monolayer HfGeTe. *Phys. Rev. Mater.* **2017**, *1*, 054003.

(15) Wieder, B. J.; Kane, C. L. Spin-Orbit Semimetals in the Layer Groups. *Phys. Rev. B: Condens. Matter Mater. Phys.* **2016**, *94*, 155108.

(16) Wieder, B. J.; Bradlyn, B.; Wang, Z.; Cano, J.; Kim, Y.; Kim, H.-S. D.; Rappe, A. M.; Kane, C. L.; Bernevig, B. A. Wallpaper Fermions and the Nonsymmorphic Dirac Insulator. *Science* **2018**, *361*, 246−251.

(17) Po, H. C.; Vishwanath, A.; Watanabe, H. Symmetry-Based Indicators of Band Topology in the 230 Space Groups. *Nat. Commun.* **2017**, *8*, 50.

(18) Kowalczyk, P. J.; Mahapatra, O.; Brown, S. A.; Bian, G.; Wang, X.; Chiang, T.-C. Electronic Size Effects in Three-Dimensional Nanostructures. *Nano Lett.* **2013**, *13*, 43−47.

(19) Scott, S. A.; Kral, M. V.; Brown, S. A. Bi on Graphite: Morphology and Growth Characteristics of Star-Shaped Dendrites. *Phys. Rev. B: Condens. Matter Mater. Phys.* **2006**, *73*, 205424.

(20) Koroteev, Y.; Bihlmayer, G.; Chulkov, E.; Blügel, S. First-Principles Investigation of Structural and Electronic Properties of Ultrathin Bi Films. *Phys. Rev. B: Condens. Matter Mater. Phys.* **2008**, *77*, 045428.

(21) Hofmann, P. The Surfaces of Bismuth: Structural and Electronic Properties. *Prog. Surf. Sci.* **2006**, *81*, 191−245.

(22) Lizzit, S.; Baraldi, A.; Grutter, Ch.; Bilgram, J.H.; Hofmann, Ph. The Surface Phase Transition and Low-Temperature Phase of α-Ga(010) Studied by SPA-LEED. *Surf. Sci.* **2009**, *603*, 3222−3226.

(23) Menteş, T. O.; Zamborlini, G.; Sala, A.; Locatelli, A. Cathode Lens Spectromicroscopy: Methodology and Applications. *Beilstein J. Nanotechnol.* **2014**, *5*, 1873−1886.

(24) Bradley, C. J.; Cracknell, A. P. *The Mathematical Theory of Symmetry in Solids*; Clarendon Press: Oxford, 1972.

(25) Xiao, C.; Wang, F.; Yang, S. A.; Lu, Y.; Feng, Y.; Zhang, S. Elemental Ferroelectricity and Antiferroelectricity in Group-V Monolayer. *Adv. Funct. Mater.* **2018**, *28*, 1707383.

(26) Murakami, S. Quantum Spin Hall Effect and Enhanced Magnetic Response by Spin-Orbit Coupling. *Phys. Rev. Lett.* **2006**, *97*, 236805.

(27) Reis, F.; Li, G.; Dudy, L.; Bauernfeind, M.; Glass, S.; Hanke, W.; Thomale, R.; Schäfer, J.; Claessen, R. Bismuthene on a SiC Substrate: A Candidate for a High-Temperature Quantum Spin Hall Material. *Science* **2017**, *357*, 287−290.

(28) Lu, Y.; Xu, W.; Zeng, M.; Yao, G.; Shen, L.; Yang, M.; Luo, Z.; Pan, F.; Wu, K.; Das, T.; He, P.; Jiang, J.; Martin, J.; Feng, Y. P.; Lin, H.; Wang, X.-S. Topological Properties Determined by Atomic Buckling in Self-Assembled Ultrathin Bi(110). *Nano Lett.* **2015**, *15*, 80−87.

(29) Fang, C.; Fu, L. New Classes of Three-Dimensional Topological Crystalline Insulators: Nonsymmorphic and Magnetic. *Phys. Rev. B: Condens. Matter Mater. Phys.* **2015**, *91*, 161105.

(30) Wang, Z.; Alexandradinata, A.; Cava, R. J.; Bernevig, B. A. Hourglass Fermions. *Nature* **2016**, *532*, 189−194.

(31) Li, S.; Liu, Y.; Wang, S.-S.; Yu, Z.-M.; Guan, S.; Sheng, X.-L.; Yao, Y.; Yang, S. A. Nonsymmorphic-Symmetry-Protected Hourglass Dirac Loop, Nodal Line, and Dirac Point in Bulk and Monolayer X_3SiTe_6 (X = Ta, Nb). *Phys. Rev. B: Condens. Matter Mater. Phys.* **2018**, *97*, 045131.

(32) Takahashi, R.; Hirayama, M.; Murakami, S. Spinless Hourglass Nodal-Line Semimetals. *Phys. Rev. B: Condens. Matter Mater. Phys.* **2017**, *96*, 155206.

(33) Yang, B.-J.; Bojesen, T. A.; Morimoto, T.; Furusaki, A. Topological Semimetals Protected by Off-Centered Symmetries in Nonsymmorphic Crystals. *Phys. Rev. B: Condens. Matter Mater. Phys.* **2017**, *95*, 075135.

(34) Hartwigsen, C.; Goedecker, S.; Hutter, J. Relativistic Separable Dual-Space Gaussian Pseudopotentials from H to Rn. *Phys. Rev. B: Condens. Matter Mater. Phys.* **1998**, *58*, 3641−3662.

(35) Gonze, X.; Beuken, J.-M.; Caracas, R.; Detraux, F.; Fuchs, M.; Rignanese, G.-M.; Sindic, L.; Verstraete, M.; Zerah, G.; Jollet, F.; Torrent, M.; Roy, A.; Mikami, M.; Ghosez, P.; Raty, J.-Y.; Allan, D. First-Principles Computation of Material Properties: The Abinit Software Project. *Comput. Mater. Sci.* **2002**, *25*, 478−492.